Earth's Future

RESEARCH ARTICLE
10.1029/2020EF001778

Increased Flood Exposure Due to Climate Change and Population Growth in the United States

D. L. Swain[1,2,3], O. E. J. Wing[4,5], P. D. Bates[4,5], J. M. Done[2], K. A. Johnson[6], and D. R. Cameron[3]

[1]Institute of the Environment and Sustainability, University of California, Los Angeles, Los Angeles, CA, USA, [2]Capacity Center for Climate and Weather Extremes, National Center for Atmospheric Research, Boulder, CO, USA, [3]The Nature Conservancy of California, San Francisco, CA, USA, [4]School of Geographical Sciences, University of Bristol, Bristol, UK, [5]Fathom, Bristol, UK, [6]The Nature Conservancy, Minneapolis, MN, USA

Abstract Precipitation extremes are increasing globally due to anthropogenic climate change. However, there remains uncertainty regarding impacts upon flood occurrence and subsequent population exposure. Here, we quantify changes in population exposure to flood hazard across the contiguous United States. We combine simulations from a climate model large ensemble and a high-resolution hydrodynamic flood model—allowing us to directly assess changes across a wide range of extreme precipitation magnitudes and accumulation timescales. We report a mean increase in the 100-year precipitation event of ~20% (magnitude) and >200% (frequency) in a high warming scenario, yielding a ~30–127% increase in population exposure. We further find a nonlinear increase for the most intense precipitation events—suggesting accelerating societal impacts from historically rare or unprecedented precipitation events in the 21st century.

Plain Language Summary Heavy rainfall is increasing globally due to human-caused global warming. However, it is still unclear how these increases in heavy rainfall might affect flood risk. In this paper, we investigate how global warming and population changes together may be affecting the number of people at risk from floods in the United States. We combine simulations from a climate model and flood model—allowing us to consider a wide range of heavy rainfall events. We report a ~20% increase in the size and a >200% increase in the frequency of very heavy and rare rainfall events, which leads to a ~30–127% increase in the number of people at risk from floods. Finally, we find that the heaviest rainfall events increase by the widest margin—suggesting the possibility of major increases in damage and disruption caused by severe floods in the 21st century.

Key Points:
- Population exposure to flood hazard is increasing due to both climate-driven increases in extreme rainfall as well as demographic shifts
- There is a wide range of plausible increases in population exposed to flood hazard, depending strongly on climate and growth scenario
- We find a nonlinear increase for most extreme events, suggesting accelerating societal impacts from historically unprecedented rainfall

Supporting Information:
- Supporting Information S1

Correspondence to:
D. L. Swain,
dlswain@ucla.edu

Citation:
Swain, D. L., Wing, O. E. J., Bates, P. D., Done, J. M., Johnson, K. A., & Cameron, D. R. (2020). Increased flood exposure due to climate change and population growth in the United States. *Earth's Future*, *8*, e2020EF001778. https://doi.org/10.1029/2020EF001778

Received 24 AUG 2020
Accepted 24 OCT 2020
Accepted article online 30 OCT 2020

Author Contributions:
Conceptualization: D. L. Swain, O. E. J. Wing, P. D. Bates, J. M. Done, K. A. Johnson, D. R. Cameron
Formal analysis: D. L. Swain, O. E. J. Wing

©2020. The Authors.
This is an open access article under the terms of the Creative Commons Attribution-NonCommercial-NoDerivs License, which permits use and distribution in any medium, provided the original work is properly cited, the use is non-commercial and no modifications or adaptations are made.

1. Introduction

Increases in heavy precipitation have long been a predicted consequence of global warming. Multiple lines of evidence—from basic thermodynamic arguments to simulations using complex coupled Earth system models—agree that the exponential increase in the water vapor-holding capacity of the atmosphere should enable a substantial increase in global precipitation extremes (Trenberth et al., 2003). Recent evidence has increasingly borne out these predictions, and increased occurrence of heavy precipitation events has now been observed both within the contiguous United States (Wright et al., 2019a) and globally (Du et al., 2019). Using newly developed climate attribution frameworks (e.g., Diffenbaugh, 2020), the detected regional and global increases in precipitation extremes have been directly linked to anthropogenic climate change (CC).

The spatial and temporal characteristics of precipitation are also expected to change in a warming climate. While global mean precipitation is projected to increase by 1–3% per degree centigrade of warming (Kharin et al., 2013), extreme precipitation is projected to increase at a much faster rate—5–10% per degree and locally higher in some regions (Pendergrass et al., 2017). Moreover, substantial changes on the dry side of the precipitation distribution are also plausible. Previous work has shown that the frequency of dry days is likely to increase across most continental regions (Polade et al., 2014) and that increases in extreme wet day frequency will largely be counterbalanced by decreased frequency of light to moderate precipitation (Thackeray et al., 2018). Collectively, these shifts are expected to result in an overall increase in hydroclimatic intensity (Giorgi et al., 2011) and an attendant increase in "precipitation whiplash" in some regions (Swain et al., 2018).

Despite this strong theoretical, numerical modeling, and observation-based evidence pointing toward increased precipitation extremes, changes in flood occurrence are subject to considerably more uncertainty. In isolation, larger or more frequent heavy precipitation events would be expected to increase the overall magnitude and/or frequency of flood events. CC-driven increases in heavy precipitation events, however, coincide with numerous other Earth system shifts that may act to diminish, or amplify, the fluvial and pluvial responses to extreme precipitation increases. Potentially confounding and possibly nonlinear influences upon potential flood hazard include decreases in antecedent soil moisture due to increased evaporation resulting from rising temperatures (Ficklin et al., 2019), increased plant water use efficiency amidst increasing atmospheric carbon dioxide concentrations (Fowler et al., 2019) and decreased cool-season and/or high elevation snowpack (Davenport et al., 2020). Direct human intervention in catchment systems, including land use change, urbanization, and flood-management infrastructure, also complicates the overall picture (Kundzewicz et al., 2014). These challenges are underscored by the fact that—despite increasingly pronounced increases in extreme precipitation—there is not yet robust observational evidence pointing to systematic increases in flood occurrence or severity (Sharma et al., 2018).

In the present analysis, we seek to characterize the response of contiguous United States (CONUS) potential flood hazard to projected increases in extreme precipitation by combining existing simulations from a climate model large ensemble and an advanced hydrodynamic flood model. In doing so, we intentionally exclude potentially confounding Earth system factors—considering the effect of projected changes in extreme precipitation in isolation. Thus, our approach offers a "zeroth order" estimate of changes in potential flood hazard due to CC—an estimate that may still be strongly modulated, regionally and seasonally, by nonprecipitation-related factors (Brunner et al., 2020).

Critically, the use of a large climate model ensemble allows for direct assessment of simulated changes in rare (and even historically unprecedented) high-magnitude precipitation extremes (i.e., those with return intervals as high as 200 years) without making any a priori assumptions regarding the underlying statistical distribution of precipitation or its stationarity over time. This represents a key strength of the present approach, as it resolves a considerable challenge faced in prior studies—which have repeatedly found that future risk estimates for historically rare events are highly sensitive to the statistical techniques used in analysis and are therefore subject to large uncertainties (e.g., Diffenbaugh et al., 2017; Lopez-Cantu et al., 2020). The large sample size afforded by numerous replications of both historical and future climate regimes in the present analysis thus allows us to quantify changes in very high-magnitude events which occur too infrequently, even in century-long empirical records or smaller climate model ensembles, to exhibit a robust signal. Additionally, our use of a high-resolution hydrodynamic model for the flood hazard component of this assessments allows us to leverage the "best of both worlds"—a large sample size from the climate model large ensemble, as well as the watershed-level specificity offered by a state-of-the-art inundation mapping tool. Details regarding this combined climate and hydrodynamic modeling approach, as well as associated caveats and major simplifying assumptions, can be found in the following section.

2. Materials and Methods

2.1. Quantifying Changes in Extreme Precipitation

Our use of a large climate model ensemble allows us to empirically quantify projected changes in rare, high-magnitude precipitation events without making parametric assumptions regarding the sparsely sampled historical record. The subsequently large sample size of simulated model-years—which includes 2,200 model-years of data for the 55-year historical period and 1,200 model-years for each of the 30-year future climate periods—allows us to empirically quantify simulated changes in precipitation events with recurrence intervals (RIs) as high as 100–200 years without using parametric curve fitting or making any a priori assumptions regarding the underlying precipitation distribution. Previous work has shown that extreme event assessment techniques that rely heavily on such parametric approaches to characterize changes in climate events for which there is little or no historical precedent are typically subject to very high uncertainty (Lopez-Cantu et al., 2020; Swain et al., 2020; Tye & Cooley, 2015), and subsequent estimates of relative risk ratios can vary widely depending on the presumed shape of the distribution (Swain et al., 2014). Thus, the use of a large ensemble coupled with relatively simple empirical analysis

of subsequent extreme precipitation occurrence represents a substantial advantage—allowing us to make stronger claims regarding the rarest and highest magnitude precipitation events with the greatest potential societal impacts.

In this study, all precipitation data are drawn from existing climate simulations using the fully-coupled Community Earth System Model (CESM 1.0) as implemented in the CESM Large Ensemble Experiment (CESM-LENS, Kay et al., 2015). This community modeling experiment explores the response of the global climate system to increased anthropogenic greenhouse gas forcing, leveraging a perturbed initial-condition ensemble ($n = 40$ members) to comprehensively characterize the wide range of natural internal variability. The ensemble includes three distinct forcing regimes: (1) a single, 1,800-year long preindustrial (circa ~1850) control run in which there are no anthropogenic climate forcings; (2) 40 replications of a twentieth century (1920–2005 of which we use data from 1950 to 2005) "historical" climate run, using perturbed initial conditions and incorporating observed anthropogenic greenhouse gas and aerosol forcings; and (3) 40 replications of projected 21st century (2005–2100 of which we use data from 2020 to 2049 and 2050 to 2079) climate assuming a high rate of anthropogenic greenhouse gas emissions (i.e., the RCP8.5 scenario), again using perturbed initial conditions.

We define two future climate regimes in this study—a "medium warming" scenario (representing the estimated climate system response to RCP8.5 emissions during the near-future 2020–2049 period during which average projected atmospheric CO_2 concentrations would be approximately ~450–500 ppm (van Vuuren et al., 2011) and a "high warming" scenario (representing RCP8.5 emissions during the more distant 2050–2079 period during which average projected atmospheric CO_2 concentrations would be approximately ~600–650 ppm). Recent work has shown that while recent socioeconomic trajectories suggest that global warming will likely be less than that which would result from the RCP8.5 socioeconomic pathway, warming and subsequent climate impact trajectories are largely scenario-independent in the near-term (i.e., through the mid-21st century) and begin to strongly diverge thereafter (Fuss et al., 2014). Thus, we intend the "medium warming" portion of the analysis to be interpreted as a plausible, high-likelihood prediction for extreme precipitation-related impacts during the 2020–2049 period irrespective of ongoing and future climate mitigation activities. The "high warming" scenario, on the other hand, may be viewed as a more speculative future scenario in which climate mitigation actions are less effective than set forth in the Paris Climate Agreement or in which amplifying natural Earth system feedbacks are stronger than currently anticipated. Plausible climate scenarios for the late 21st century likely fall in between the "medium" and "high" warming scenarios set forth here—and thus, it would be reasonable to assume that impacts upon extreme precipitation and potential flood hazard would fall somewhere in between these two scenarios (Fuss et al., 2014; Rogelj et al., 2016).

We first use daily, all-season precipitation data from CESM-LENS to quantify the magnitude of simulated extreme events during the historical period for a wide range of event magnitudes (RIs of 5, 10, 20, 50, 100, and 200 years) and precipitation accumulation time horizons (1, 2, 3, 5, 7, 14, and 28 days) on a grid point basis for the CONUS. Once we have calculated the precipitation value associated with each magnitude and duration combination at each climate model grid point, we compare these historical reference values to those during the preindustrial and future "medium" and "high" warming scenarios (Figure 1). Changes in event magnitude are assessed as absolute differences in the actual precipitation value associated with the ith RI and jth accumulation time horizon during each period. Changes in event frequency are assessed using a "peaks over threshold" approach, empirically counting exceedances of the historical precipitation value associated with the ith RI and jth accumulation time horizon during each period (Figures 2 and 3).

To ensure statistical robustness, we employ a bootstrap resampling approach at two points in the analysis. First, to obtain the baseline precipitation values associated with the ith RI and jth accumulation time horizon in each of the $n = 40$ ensemble members, we randomly subsample (with replacement) individual days (or consecutive multiday periods) from each period in each member to calculate $m = 25$ distinct estimates of the associated precipitation values. Precipitation values from the resulting subsample are then arranged in descending order, and pseudo-empirical estimates of the quantiles associated with specific RIs are calculated. Then, after the $m * n = 1{,}000$ bootstrap iterations have been completed, all model-years are pooled across the 40 ensemble members in each period separately for each climate regime (i.e., preindustrial,

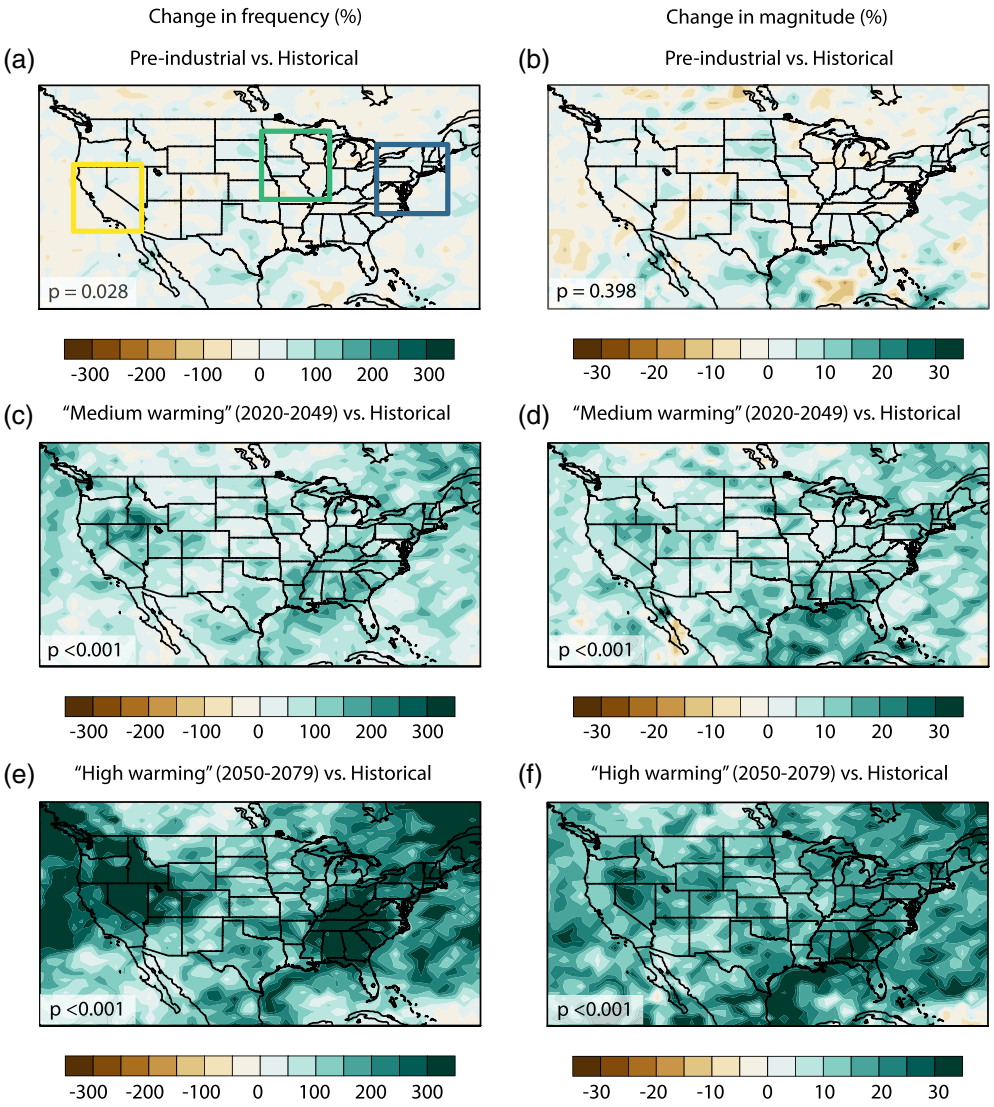

Figure 1. Change in extreme precipitation occurrence, CESM-LENS. Left column: relative (%) change in frequency of exceedance of the 1-day precipitation accumulation associated with a 100-year RI under three different climate forcing regimes as simulated in CESM-LENS. Right column: same as left, except plotted values depict relative changes in magnitude (vs. frequency). In both columns, changes are calculated using a fixed 1950–2005 baseline for 1-day precipitation accumulations. Yellow, green, and blue regional boxes in (a) are bounding boxes for the Pacific Southwest, Upper Mississippi, and Eastern Seaboard regions, respectively.

historical, medium warming, and high warming). In the final step, the precipitation values across all 1,000 iterations are averaged, with the resulting lat/lon array of values for each *i*,*j* combination taken as the final estimate.

All *p* values in this analysis are the product of two-tailed Student's *t* tests, which test the null hypothesis that the means of two populations are statistically indistinguishable. Differences in CONUS-wide changes in extreme precipitation frequency and intensity are assessed as the difference between climate regimes (e.g., high warming vs. historical) across all CONUS grid boxes (defined as a nominally rectangular region bounded by 30°N, 50°N and 125°W, 65°W and including both land and ocean grid boxes within these bounds) in each period. For all CONUS-wide values, individual grid box values are weighted by the cosine of latitude.

2.2. CESM "fitness for purpose"

As with all experiments involving climate model simulations, the degree of fidelity in representing extreme precipitation events is an important consideration. Present-generation climate models, most of

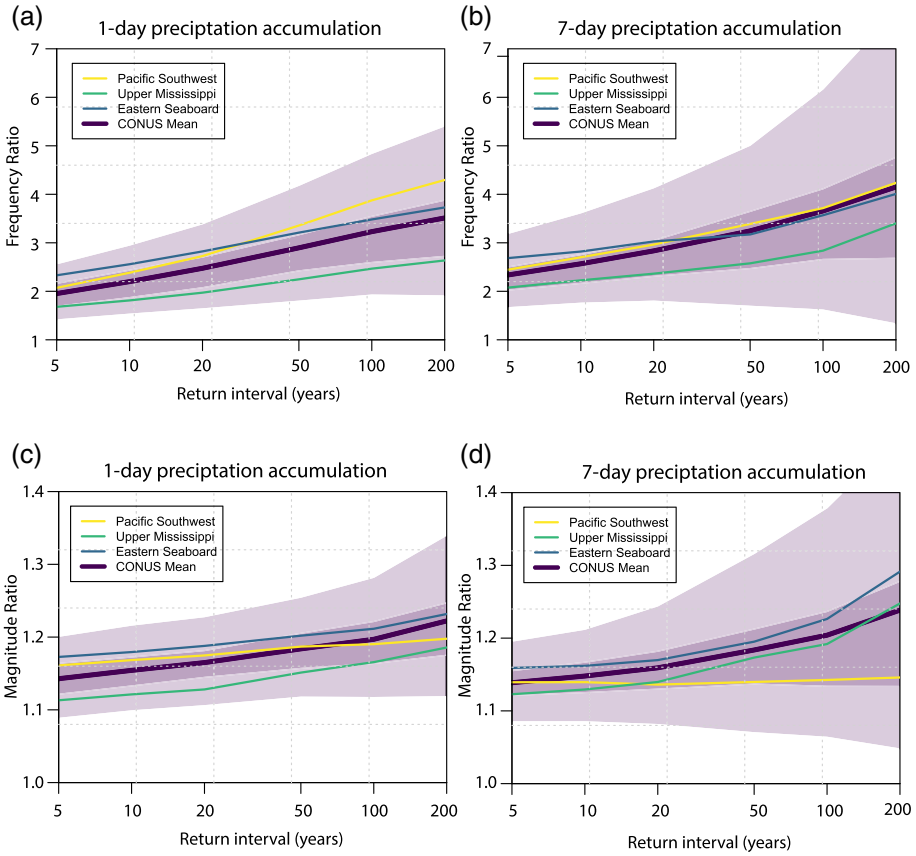

Figure 2. Change in extreme precipitation occurrence as function of event magnitude. (a) Ratio of frequency of exceedance of extreme 1-day precipitation accumulations under a high emissions scenario (RCP8.5 during 2050–2079) to that during the historical period (1950–2005) as a function of event magnitude (i.e., return interval). (b) Same as (a) but for 7-day precipitation accumulations. (c) Ratio of magnitude of extreme 1-day precipitation accumulations under a high emissions scenario (RCP8.5 during 2050–2079) to that during the historical period (1950–2005) as a function of event magnitude (i.e., return interval). (d) Same as (c) but for 7-day precipitation accumulations. In all panels, the thick purple line denotes the average value across all CESM-LENS grid boxes across CONUS; the green, blue, and yellow lines denote regionally averaged values in specific subregions, and the light (dark) purple shading denotes the upper/lower tercile (10th/90th) percentile bounds for values across all CONUS grid boxes. Ratios greater than 1 denote an increase in frequency/magnitude; all horizontal axes are logarithmic.

which have relatively coarse (~100–200 km) spatial resolution, have difficulty in representing short-timescale (i.e., subdaily) and/or convective extreme precipitation events—which must be indirectly parameterized, rather than explicitly represented. These challenges can be mitigated through the use of high-resolution and/or convection-permitting, nonhydrostatic models (Prein et al., 2017). The heavy computational burden of such simulations, however, means that large ensembles of nonhydrostatic model simulation do not yet exist—although recent analyses have attempted to bring together the "best of both worlds" by conducting targeted dynamical downscaling nested within large ensembles (Huang et al., 2020).

Given this reality, we therefore ask: Can CESM-LENS provide a sufficiently good estimate of present-era and future precipitation extremes for the purposes of providing a first-order estimate of changes in continental-scale flood potential? Precipitation simulated by CESM1 has been previously validated against remotely sensed satellite (TRMM) observations in a global context (Norris et al., 2019) and against gauge-based in situ observations in a regional context (e.g., Swain et al., 2018). In general, such comparisons have suggested that CESM1 offers a reasonable representation of global patterns in both mean and extreme precipitation, though with substantial regional biases in some cases. Globally, CESM simulated extreme precipitation exhibits slight positive biases in the tropics and slight negative biases in the midlatitudes (+4% and −4%,

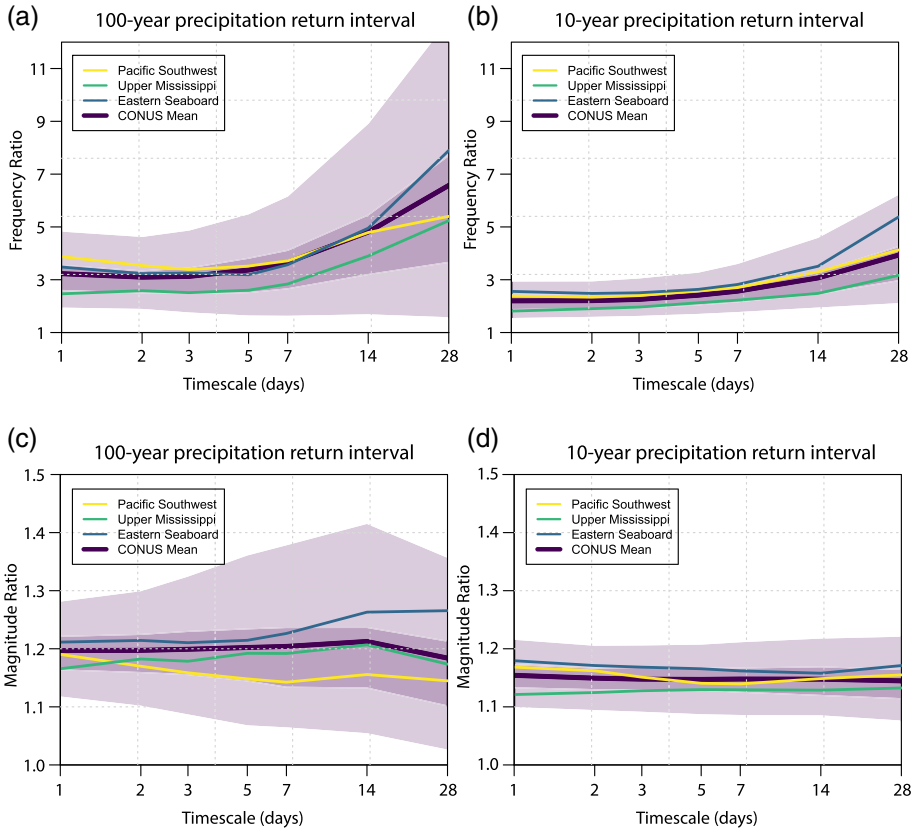

Figure 3. Change in extreme precipitation occurrence as function of event duration. (a) Ratio of frequency of exceedance of extreme (100-year RI) accumulations under a high emissions scenario (RCP8.5 during 2050–2079) to that during the historical period (1950–2005) as a function of event duration (i.e., timescale of precipitation accumulation). (b) Same as (a) but for 10-year RI events. (c) Ratio of magnitude of extreme (100-year RI) precipitation accumulations under a high emissions scenario (RCP8.5 during 2050–2079) to that during the historical period (1950–2005) as a function of event duration (i.e., timescale of precipitation accumulation). (d) Same as (c) but for 10-year RI events. In all panels, the thick purple line denotes the average value across all CESM-LENS grid boxes across the CONUS; the green, blue, and yellow lines denote regionally averaged values in specific subregions, and the light (dark) purple shading denotes the upper/lower tercile (10th/90th) percentile bounds for values across all CONUS grid boxes. Ratios greater than 1 denote an increase in frequency/magnitude; all horizontal axes are logarithmic.

respectively, for the 6-hour accumulation with 10-year local RI (Norris et al., 2019). This likely reflects the higher fraction of resolved large-scale precipitation (as opposed to unresolved convective precipitation) at higher latitudes versus lower latitudes (Pendergrass et al., 2019).

Multiple studies have noted that, within the CONUS, CESM precipitation exhibits relatively low biases across the western half of the United States (including the Pacific Coast (Swain et al., 2018) but higher (dry) biases in the east—particularly in the southeastern United States (Norris et al., 2019). Previous work has shown that the inability to resolve propagating mesoscale convective systems, which are responsible for a substantial fraction of extreme precipitation across portions of the central United States, may play a role in these biases east of the Rocky Mountains (Prein et al., 2017). While the underlying CAM5 dynamical core in CESM has been shown to reasonably represent tropical cyclone-associated precipitation in aggregate (Villarini et al., 2014), other work has suggested that the spatial structure of tropical cyclones and associated precipitation in 1° models such as CESM is not always realistic (Bacmeister et al., 2018). This may be an important caveat in places where the contribution of tropical cyclones to precipitation extremes is important, such as along the Gulf Coast and in the southeastern United States. Additionally, we also acknowledge the long-standing "drizzle problem" in coarse-resolution atmospheric models, which results in simulated precipitation that is too frequent but insufficiently intense (e.g., Kay et al., 2018; Stephens et al., 2010). However, biases in CESM-LENS specifically appear to be much lower for higher magnitude and

longer-duration magnitude precipitation events, increasing confidence that CESM-LENS is an appropriate tool for studying precipitation extremes on broad spatial scales and multiday timescales (Norris et al., 2019). We further note that the "change factor" approach used in the present study—which quantifies only the relative, internally consistent simulated changes in extreme precipitation—also acts as a form of implicit bias correction by de-emphasizing the importance of CESM's background precipitation climatology in assessment metrics.

2.3. Hydrodynamic Modeling Using Fathom-US

The hydrodynamic flood inundation model used in this analysis, Fathom-US, produces spatially continuous flood hazard maps of the entire CONUS. The model was first presented and validated in Wing et al. (2017), based on the global flood model building methodology of Sampson et al. (2015) and simulates both fluvial and pluvial flooding. We emphasize that no new hydraulic model components are introduced in the present study beyond those which have been previously described and validated. Extreme river flows are computed using a regional flood frequency analysis (RFFA) of U.S. Geological Survey stream gauges, based on the global RFFA (Smith et al., 2015) and generally covering the ~1960–2010 period. These fluvial model boundary conditions are routed in 1D through subgrid-scale river channels based on HydroSHEDS hydrography data (Lehner et al., 2008; Neal et al., 2012). The computational hydraulics are based on LISFLOOD-FP, which numerically solves a local inertial formulation of the shallow water equations in 2D for out-of-bank flows and in 1D for in-channel flows (Bates et al., 2010; de Almeida et al., 2012; Neal et al., 2012). Elevation data are sourced from the 1 arc second (~30 m) resolution U.S. Geological Survey National Elevation Dataset, with hydraulic simulations executed at this native resolution. Known flood defenses are incorporated explicitly into the model and are sourced from the U.S. Army Corps of Engineers National Levee Database.

The fluvial model is executed for all rivers with a drainage area exceeding 50 km^2. Small headwater catchments, as well as surface water flooding, are simulated by the pluvial model. The pluvial model component retains the features of the fluvial model, except the river flow boundary conditions are replaced by precipitation inputs which fall directly onto the elevation grid (Sampson et al., 2013). The rainfall inputs are defined using Intensity-Duration-Frequency relationships from NOAA. Infiltration rates are computed based on soil data, while standards of drainage capacity are assumed based on degree of urbanization.

The model thus produces 17 CONUS-wide fluvial and pluvial flood hazard maps, ranging return periods from 1 in 5 years to 1 in 1,000 years (20–0.1% annual exceedance probability). The model has been rigorously validated against engineering-grade, local-scale flood models and against observations of real flood events (Emanuel, 2017; Wing et al., 2017; Wing et al., 2019; Wing et al., 2019). Correspondence between the flood extents simulated by Fathom-US and those of benchmark data sets in these studies amounted to a 70–90% fit (accounting for both overprediction and underprediction), approaching a performance ceiling given likely errors in the benchmarks themselves.

2.4. Connecting Extreme Precipitation and Flood Potential Exposure

Precipitation simulations from CESM-LENS were converted to spatially explicit gridded data describing the relative change in magnitude of extreme precipitation events with RIs of 1 in 5, 10, 20, 50, 100, and 200 years over accumulation lengths of 1, 2, 3, 5, 7, 14, and 28 days across the CONUS. These "change factors" were generated for preindustrial (c ~ 1850), "medium warming" (RCP8.5 2020–2049), and "high warming" (RCP8.5 2050–2079) scenarios relative to the historical (1950–2005) CESM-LENS simulation. These changes were used to perturb the underlying boundary conditions of the Fathom-US model, permitting the generation of new return period flood hazard maps for each scenario via extraction from the precomputed (historical) catalog. This extraction is performed in a hydrologically consistent manner, where the existing inundation depths are discretized into river catchments defined by HydroBASINS (level 10 from Lehner & Grill, 2013).

For the fluvial model, the characteristics of the river cell at each river catchment outlet initially determine which rainfall accumulation length to consider. Larger river flooding is dependent upon longer periods of rainfall, while headwater streams respond to short-duration rainfall. A time to concentration (Tc) at each outlet is therefore estimated based on Manning's equation and unpaved shallow concentrated flow velocities set out in USDA (1986). This Tc stipulates which rainfall accumulation length to consider for each

catchment (see full Tc distribution in supporting information Figure S1b). The mean precipitation change factor for a given return period, as derived from CESM-LENS, is then sampled from all cells upstream of a given river catchment outlet. Using the RFFA-defined flood frequency curve for this river, the given return period flow magnitude is perturbed by the precipitation change factor. The return period of this new river discharge, with respect to the historical RFFA, is then computed, and the corresponding return period flood hazard map is extracted.

As an example, consider how catchment *A*'s 100-year flow of 500 $m^3 s^{-1}$ might change by 2079. The estimated Tc to catchment *A*'s outlet is 4.8 days, so we consider the changes to the 100-year 5-day rainfall accumulation in the 2050–2079 time horizon. The mean change factor for the 100-year rainfall upstream of catchment *A*'s outlet is 15%, meaning the 100-year flow by 2079 at this point is projected to be 575 $m^3 s^{-1}$. This new 100-year flow corresponds to the historical 200-year flow in catchment *A*, as defined by the RFFA. Since we have already simulated the 200-year flow, we simply extract the inundation depths in catchment *A* from this simulation and stitch it into a new 2050–2079 100-year CONUS flood map. This is repeated for all CONUS river catchments, where different historical return periods are extracted for each catchment depending on the relevant duration rainfall change factors.

For the pluvial model, only 1-day rainfall accumulation changes are considered. This is the shortest accumulation length considered in the climate portion of the analysis, and we also note that pluvial floods are generally characterized by rapid responses to brief but intense downpours. The mean change factor is computed within each catchment (not all areas upstream), and a similar process is performed as with the fluvial model, except that changes are referenced to the Intensity-Duration-Frequency curves of the input rainfall.

The result of these processes is the production of multiple ~30 m resolution, CONUS-wide, fluvial and pluvial, return period flood hazard maps for each scenario. To compute potential flood exposure, populations residing in inundated cells for each map are summed. For the present day, a ~30 m dasymetric map of population based on census counts and high-resolution land-use data from the U.S. Environmental Protection Agency (USEPA) EnviroAtlas program is employed. For future scenarios, existing gridded projections of population from the USEPA Integrated Climate and Land-Use Scenarios (ICLUS) project are employed. In ICLUS, these future population projections are generated using a demographic model to estimate county-level population changes, which are then distributed to housing units using a 90 m resolution spatial allocation model. The underlying demographic model accounts for fertility, mortality, and migration, projecting county counts of population cohorts split by ethnicity, age, and gender. The spatial allocation model primarily requires existing housing unit and population data, undevelopable lands, commercial and industrial land use, transport networks, and groundwater well density to distribute the county-level projections based on assumptions related to travel times, household size, and land-use demand. In the present analysis, we have chosen a single "medium growth" scenario from ICLUS (SSP2), which closely tracks population projections of the U.S. Census Bureau. These population projections are based on a host of assumptions, including (a) the continuation of historical migration patterns, (b) land use changes which are consistent with historical land-use transitions (e.g., expansion versus densification of cities), and (c) historical demands for amenities and transport capacity. These population projections therefore represent a single plausible realization of future U.S. demographic conditions drawn from infinitely many possibilities based on model parameters grounded in historical data. More details may be found in USEPA (2016).

2.5. Caveats and Simplifying Assumptions

This analysis considers the flood *potential* of a changing climate by equating changes in rainfall and changes in river flows, as is common in large-scale flood hazard projections (e.g., Uhe et al., 2019). The method considers only catchment size and rainfall changes in its determination of inundation scenarios, assuming that the antecedent conditions and flood drivers that are not explicitly modeled (e.g., snowpack and antecedent soil moisture) remain consistent with historical observations. This represents a substantial simplifying assumption, as it has been previously demonstrated that flood response to extreme precipitation is strongly modulated by a variety of nonprecipitation factors on a seasonally and regionally varying basis, many of which are expected to change in a warming climate (e.g., Brunner et al., 2020). However, the simple framework we employ here provides an efficient means for the estimation of flood impacts at the contiguous scale —essentially examining a CC-adjusted version of historical CONUS flood events based on projected changes

in extreme precipitation. Ultimately, this allows us to quantify the idealized "zeroth order" effect of changes in extreme precipitation to flood potential hazard and to isolate the effect of extreme precipitation from other nonstationary climate variables.

Finally, we note that the hydrodynamic modeling approach used in the present study presumes structural integrity of existing flood control infrastructure such as dams and levees under very extreme conditions. This means that while inundation due to dam/levee overtopping is accounted for, inundation resulting from potential structural failure or collapse is not (contrarily, we also acknowledge that our methods may underestimate the level of protection offered by flood defense structures not included in the underlying USACE database). Recent events—including the near-catastrophe at California's Oroville Dam in 2017 and the devastating regional flooding caused by levee and dam failures in the Upper Midwest (in 2019) and in Michigan (in 2020)—signal that existing water infrastructure is already at risk during sufficiently severe precipitation events in the present climate and that catastrophic failures can indeed occur. Thus, in light of the widespread increase in precipitation extremes reported herein and the fact that our modeling approach cannot quantify further increases in risk from possible levee and/or dam failures, the inundation maps and population exposure estimates presented do not necessarily represent worst-case estimates of the flooding that could potentially result from very high magnitude (100- to 200-year RI or greater) precipitation events. Quantifying these additional risks from possible levee and/or dam failures is beyond the scope of this manuscript but should be urgently considered in future research and in developing climate adaptation/emergency response plans.

3. Widespread Simulated Increase in Extreme Precipitation

We find widespread and substantial increases in simulated extreme precipitation events in two both future climate scenarios with elevated levels of anthropogenic greenhouse gas forcing, but these increases do not clearly emerge until after the twentieth century historical climate period across the CONUS. We report small, regionally heterogeneous, and statistically weak changes in the frequency of occurrence (CONUS average = −2.4%, $p = 0.028$ for ~100-year RI event) and magnitude (CONUS average = −1.0%, $p = 0.398$) of extreme precipitation events during the historical period (1950–2005) relative to the preindustrial period (c. 1850, Figures 1a and 1d). This suggests the lack of a systematic signal regarding changes in high-magnitude precipitation events during the latter half of the twentieth century.

A much stronger signal emerges in both future climate scenarios which include greenhouse gas emissions substantially above twentieth century levels. In the near-term/medium emissions future (2020–2049) simulations (see Methods for formal definition of "medium" and "high" emissions scenarios), widespread increases in extreme precipitation frequency (CONUS average = +87.1%, $p < 0.001$) and magnitude (CONUS average = +10.5%, $p < 0.001$) are apparent across nearly the entire CONUS, Figures 1b and 1e), with frequency increases locally exceeding 200% and magnitude increases exceeding 20%. In the long-term/"high emission" future simulations (2050–2079), large increases in both the frequency (CONUS average = +223.0%, $p < 0.001$) and magnitude (CONUS average = +19.7%, $p < 0.001$) of precipitation occur across the entire domain, with large regions experiencing frequency increases exceeding 300% (i.e., a three-fold increase) and magnitude increases exceeding 25% (Figures 1c and 1f).

We find that the largest projected increases in the magnitude of 100-year precipitation events occur over portions of the Gulf Coast states and southeastern United States more broadly. Strikingly, this includes portions of Texas, Louisiana, and both North and South Carolina—regions that have all experienced catastrophic floods between 2015 and 2020 resulting from slow-moving tropical cyclones (Touma et al., 2019) that produced extreme precipitation events greatly exceeding historical 100-year RIs (Emanuel, 2017). Large increases in the frequency of 100-year precipitation events occur across a broader region encompassing most of the southeastern United States and Eastern Seaboard, as well as a broad portion of the western United States extending from the Pacific coast to the western Rocky Mountains. This latter region includes California—a state previously identified as being at high risk of increased future precipitation extremes as a result of warmer, moister atmospheric river storms (Huang et al., 2020; Swain et al., 2018). In sum, the CESM Large Ensemble projects large increases in both frequency and intensity of high-magnitude precipitation events across a wide range of underlying climatological regimes and precipitation-generating processes.

3.1. Largest Increase for Rarest, Highest Magnitude Events

We assess changes in simulated extreme precipitation across a range of event magnitudes (RIs of 5–200 years). Here, we focus on the "high warming" climate scenario to achieve the strongest signal-to-noise ratio. We find that virtually all CONUS grid points exhibit positive increases in both event frequency and magnitude (see tenth percentile bounds, Figures 2a–2d and 3a–3d) at all timescales, but the margin of exceedance of historical thresholds increases monotonically with increasing event magnitude. As a result, the greatest precipitation increases occur for extremely high magnitude events, that is, those with historical RIs of 50–200 years. In the CONUS average, for instance, the relative increase in frequency of the 200-year RI event (for 1-day accumulations) is more than double that of the 5-year RI event (frequency ratio of 3.5 vs. 2.0 in Figure 2a, corresponding to a 250% vs. 100% increase, respectively). This is similar to results using 7-day precipitation accumulation windows (Figure 2b), where the increase in frequency for the 200-year event is also more than double that of the 5-year event (+315.1% vs. +133.7% increase, respectively). For changes in the magnitude of precipitation associated with events of a given frequency (i.e., using fixed RIs in future vs. historical periods), we again find progressively larger increases in precipitation intensity with increasing event magnitude—although the margin of this increased scaling by event size is smaller than for frequency changes (Figures 2c and 2d vs. 2a and 2b). The 1-day accumulation window, for instance, yields magnitude increases ranging from +14.3% (for the 5-year event) to +22.2% (for the 200-year event).

We next assess changes in simulated extreme precipitation across a range of event durations (precipitation accumulation timescales of 1–28 days). Here, we once again report absolute increases in event magnitude and frequency at all timescales for virtually all grid boxes (Figure 3). From a frequency perspective, these increases are essentially flat for accumulation timescales of 1–5 days (frequency ratio of ~3.1, corresponding to a 210% increase, for the 100-year event CONUS mean) but begin to rise sharply for accumulation timescales greater than 7 days (frequency ratio rising as high as 6.6, corresponding to a 560% increase, at 28-day timescales, Figures 3a and 3b). From a magnitude perspective, however, the rate of increase across accumulation timescales is quite flat (magnitude ratio ~1.2 for both the 100-year event and the 10-year event).

The fact that frequency and magnitude-based metrics of extreme precipitation increase are consistent when assessed as a function of event magnitude but diverge when assessed as a function of event duration is worth further discussion. In general, empirical and simulated precipitation distributions are non-Gaussian and exhibit heavy upper tails (Papalexiou et al., 2013). One consequence of such a distribution is that, for events sufficiently far in the upper tail, even modest increases in the relative magnitude can equate to large, nonlinear increases in frequency. This intrinsic statistical property of heavy-tailed precipitation distributions thus may partially explain the divergence between the flatness of Figures 3c and 3d and the steepness of Figures 3a and 3b. The physical interpretation in this instance is intuitive: the absolute amount of precipitation occurring during long-duration (28 days) events is much larger than during short-duration (1 day) events—meaning that a 15–20% increase in precipitation accumulation equates to both a larger absolute increment of precipitation increase and a statistically much rarer event at long timescales.

In contrast to the event duration results, however, both frequency and magnitude scaling are strongly positive as a function of event intensity. Not only is the absolute increment of precipitation increase larger for higher intensity events, but the *rate of increase* of the precipitation increment (i.e., the second derivative of precipitation as a function of magnitude, d^2P/d^2P_m) itself increases as a function of event magnitude ($d^2P/d^2P_m > 0$). The monotonic increase in event frequency as a function of event intensity, therefore, is unlikely to be solely explained by a simple upward shift in the mean of the underlying heavy-tailed precipitation distribution. Indeed, this simulated nonlinear "acceleration" of future changes in precipitation as a function of event intensity has previously been identified in CESM-LENS and a subset of other global climate models (Mizuta & Endo, 2020), mainly in the tropics (Pendergrass et al., 2019). The present results are drawn from a mainly midlatitude domain—suggesting that a similar phenomenon also exists outside of the tropics, and across the CONUS specifically, at sufficiently extreme event thresholds (i.e., 50- to 200-year RI events). Norris et al. (2019) found a similarly large and nonlinear increase in simulated extreme precipitation in CESM-LENS across a global domain and also demonstrated that the primary mechanism for such increases is a thermodynamically driven increase in atmospheric moisture. However, this moisture increase was

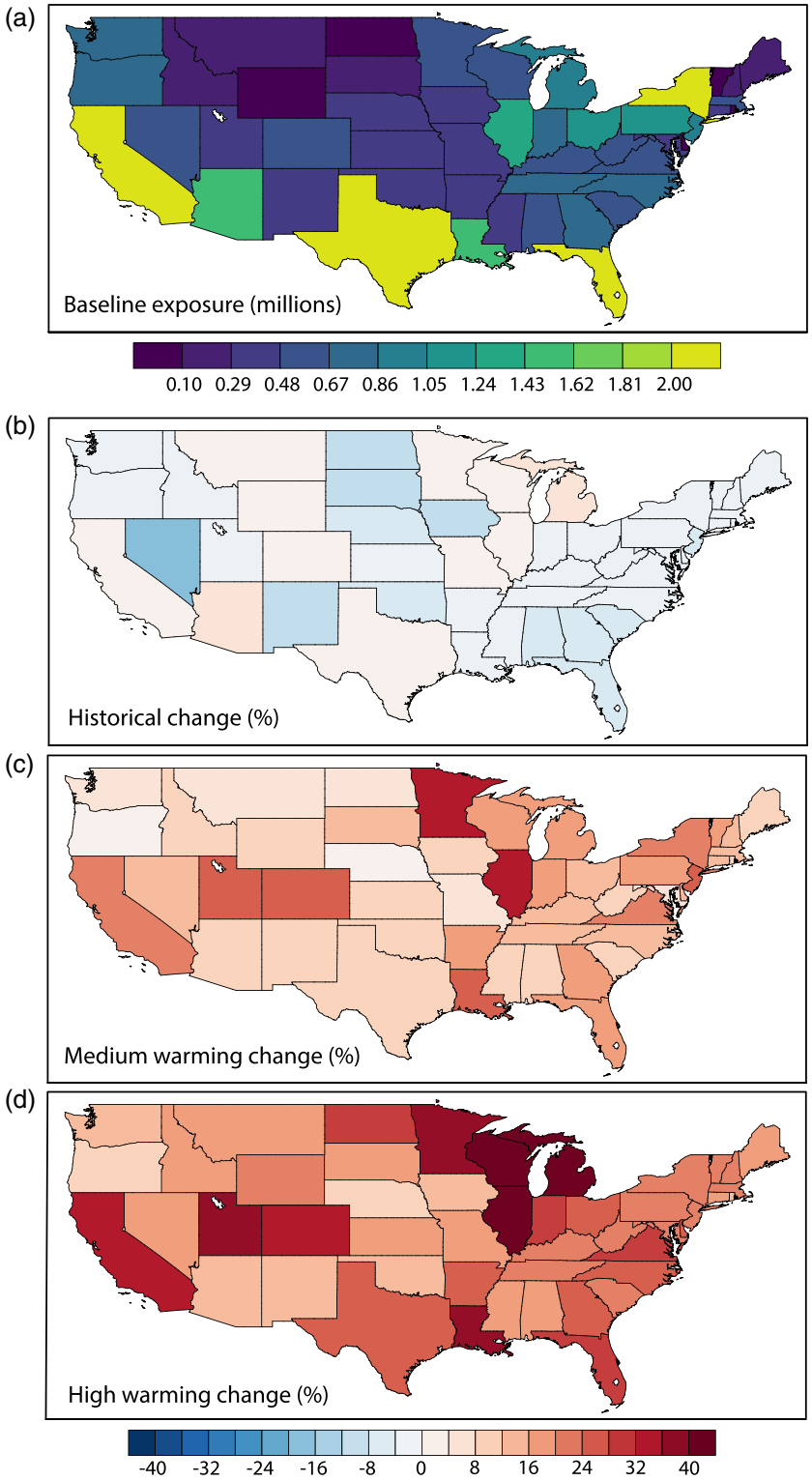

Figure 4. Change in population exposure to extreme flood potential due to climate change. (a) Population living within 100-year floodplain (for freshwater inundation) under preindustrial (circa ~1850) climate conditions (in millions). (b) Change in population living within 100-year floodplain for historical (1950–2005) relative to preindustrial climate conditions. (c) Change in population living within 100-year floodplain for medium emissions future scenario (RCP8.5 2020–2049) relative to preindustrial climate conditions. (d) Change in population living within 100-year floodplain for high emissions future scenario (RCP8.5 2050–2079) relative to preindustrial climate conditions. In all panels, population is held constant at present-day (~2010) levels and spatial distribution.

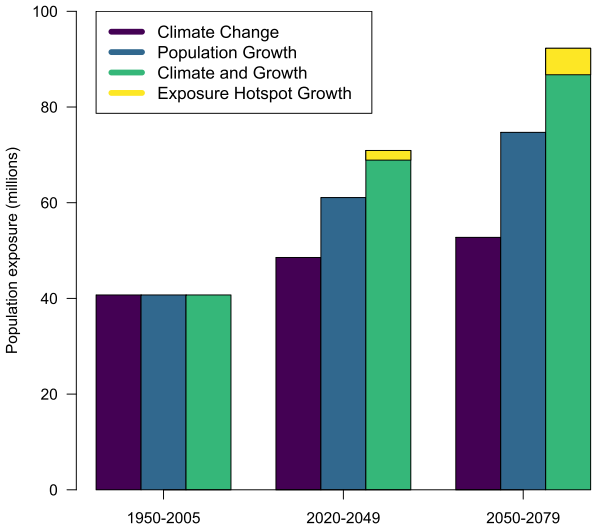

Figure 5. Contributions of climate and demographic changes to 100-year flood exposure. Projected population exposure to extreme flood events (100-year RI) given projected climate-driven changes in extreme precipitation only (purple columns), projected population growth only (blue columns), and both climate and population growth together (sum of stacked green and yellow columns). Yellow portion of the rightmost column denotes "nonlinear" portion of total increase in population exposure exceeding that which would result from the simple addition of climate and population changes in isolation (i.e., population growth in "exposure hotspots").

modulated in a regionally varying manner by changes in extreme event duration—amplifying precipitation extremes in the midlatitudes and dampening them in the tropics.

Collectively, these complex precipitation scalings along magnitude and duration axes have potentially large practical implications for climate adaptation and infrastructure design purposes. Precipitation changes inferred directly from the relatively short historical record—and/or short-running/small ensemble climate model simulations—generally cannot be used to robustly characterize changes in very high magnitude precipitation extremes (Lopez-Cantu et al., 2020). As a result, traditional analysis methods may substantially underestimate the increase in very high magnitude and/or very long-duration precipitation events—precisely those which present the greatest risk of harmful flooding to urban areas and critical infrastructure. Moreover, this aspect of our findings appears to hold across a wide range of geographic and climatological regimes. This is illustrated by the similarity between the yellow, green, and blue regional curves in Figures 2 and 3—which correspond to the bounding boxes in Figure 1a denoting the Pacific Southwest, Upper Mississippi, and Eastern Seaboard regions, respectively.

The nonlinearity and spatial pattern of these precipitation scalings may also offer preliminary insights into underlying mechanisms. Numerous previous studies have reported that warming-induced increases in simulated extreme precipitation are larger than would be expected from Clausius-Clapeyron scaling alone (i.e., ~7% per degree C of warming)—especially for short-duration convective events (e.g., Prein, Liu, Ikeda, Trier, et al., 2017) and for at least certain types of non-convective events, such as landfalling atmospheric river storms (Huang et al., 2020). Our results suggest that regional maxima of extreme precipitation increase occur along the Gulf Coast/southeastern United States and along the Pacific Coast (Figures 1e and 1f)—regions where convective storms and atmospheric rivers, respectively, are indeed responsible for a large fraction of the most intense precipitation events (Touma et al., 2018).

At short timescales, these accentuated increases may arise from increased horizontal moisture convergence in a warmer/wetter atmosphere (e.g., Lenderink et al., 2017). Over longer accumulation timescales, Neelin et al. (2017) found that increases in the variability of moisture convergence—combined with the existence of fixed moisture thresholds associated with event initiation and termination—yielded preferentially large increases in the largest and historically rarest precipitation events. Increases in the spatial extent of extreme precipitation (Lenderink et al., 2017; Lochbihler et al., 2019) and/or decreases in the horizontal translational speed of specific types of extreme precipitation-generating events, such as tropical cyclones in the midlatitudes (e.g., Kossin, 2018; Zhang et al., 2020), could also contribute to the nonlinear increase in the highest magnitude events we report here (Figure 2). Moreover, Thackeray et al. (2018) demonstrated a global precipitation "compensation effect," whereby future precipitation increases are concentrated temporally into the most intense events at the expense of weaker events. This suggests that the accelerated increase in event magnitude at the highest intensities shown in the present analysis may be linked to a more fundamental aspect of the global climate response. A comprehensive assessment of these diverse phenomena and possible physical drivers is beyond the scope of this study, but will be the focus of future work.

4. Changing Climate and Demography Drive Increased Flood Exposure

Although changes in population exposure to 100-year RI flood events due to historical CC (1950–2005) are modest and spatially heterogeneous, we find that much larger and more widespread increases occur in both medium and high future warming climate scenarios (Figure 4). During the historical period, modern-day population exposure changes are generally small (Table S1; Figure 4b). These relatively weak trends during the historical period, which encompass both increases and decreases in population exposure on a statewide basis, likely reflect relatively weak external forcing compared to future scenarios. Large increases in

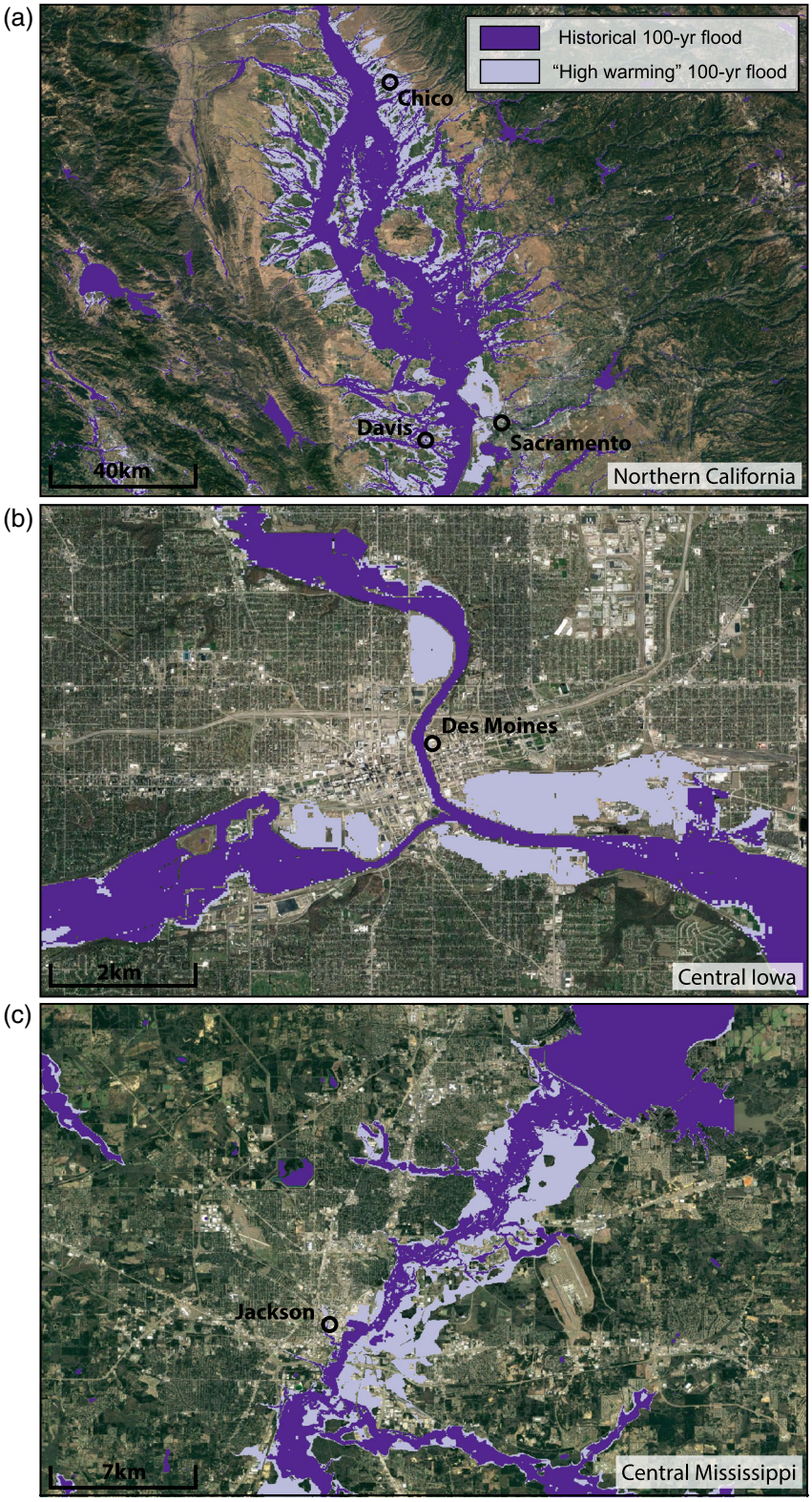

Figure 6. Change in 100-year flood inundation for selected locations. Inundation maps derived from hydrodynamic model depicting estimated flood extent resulting from an extreme precipitation event with an approximately 100-year RI in the historical climate (1995–2005, dark purple shading) and a "high warming" climate scenario (RCP 8.52050–2079, light purple shading). Locations depicted include (a) the Sacramento Valley in northern California including the Sacramento River, (b) the confluence of the Des Moines River and Raccoon River near Des Moines in central Iowa, and (c) the Pearl River near Jackson, Mississippi. Additional inundation maps may be found in Figure S2.

population exposure, however, quickly emerge in most U.S. states by mid-century (2020–2049) in the medium warming scenario even when total population is held constant (Figure 4b). In the high warming scenario—which could occur later during the 21st century (2050–2079)—population exposure continues to increase, with five states (Florida, California, Texas, Illinois, and Louisiana) experiencing cumulative exposure increases exceeding 0.5 million people (Table S1). We emphasize that while absolute population exposure increases virtually everywhere due to widespread increases in extreme precipitation in both medium and high warming scenarios, it is clearly most concentrated in states with the highest preexisting risk (Figure 4a). In relative terms, statewide increases in population exposure range from a low of +3.6% in Oregon to a high of +32.8% in Minnesota under the medium warming scenario and from +11.8% in Oregon to +48.9% in Illinois under the high warming scenario (Figure 4c).

In Figure 5, we partition the effects of simulated CC (i.e., increases in extreme precipitation) and projected human development patterns (i.e., increases in population and changes in spatial distribution) upon population exposed to the "100-year flood." Assuming no change in total population, we find that CC increases CONUS-wide potential flood exposure by 7.83 million (+19.2%) under the medium warming scenario and 12.04 million (+29.5%) under the high warming scenario—and more than doubles exposure in a high warming, high population growth (PG) scenario by 2050–2079 (+126.6%). Meanwhile, projected PG alone, in the absence of CC, would yield an exposure increase of 20.35 million and 33.98 million using mid-century and late-century estimates, respectively.

Yet, surprisingly, we find that the combined effects of CC and PG are not simply additive. In both the medium and high warming scenarios, the total population exposure increase is substantially greater than would be estimated from the simple sum of CC and PG (by 2.02 million for the medium warming scenario and 5.53 million for the high warming scenario). The nonlinear increase can be attributed to "exposure hotspots"—regions that were neither within the historical 100-year flood plain nor substantially populated during the twentieth century but subsequently fall within the expanded 21st century floodplain and experience projected population expansion during the same interval. In other words, these exposure hotspots quantify the flood exposure increment contributed by future population expansion into new inundation zones caused by CC. To illustrate the greatly expanded 100-year flood footprint in a warmer 21st century versus historical climate and its extent relative to nearby major population centers, we compare estimated inundation maps of several specific regions (including the Sacramento and San Joaquin valleys in California, central Iowa, central Mississippi, northern Missouri, and eastern Georgia) in Figures 6 and S2. Finally, we quantify this hotspot effect at the individual state level. We find the largest absolute hotspot population exposure increases (>500,000 people per state in a high warming scenario) across the most populous "Sunbelt" states of California, Texas, and Florida. However, the largest relative increases in hotspot exposure (exceeding 15% of the total exposure increase in a high warming scenario) occur in quite different regions—including the southeastern Atlantic coast states of Georgia, North Carolina, and South Carolina; the Upper Midwest states of North Dakota and South Dakota; and portions of the Intermountain West (especially Nevada) (Figure S3).

5. Conclusions

We find that substantial increases in the occurrence of extreme precipitation events and subsequent population exposure to potential flood hazard are essentially inevitable over the near-term (i.e., over the next 30 years) across the CONUS and may continue to rise thereafter depending on the real-world trajectory of greenhouse gas emissions. A larger increment of the increases in climate-driven increases in population exposure occur during the earlier (2020–2049) period versus later (2050–2079) period—suggesting that there is a relatively large population in areas in close proximity to present-day floodplains that is highly vulnerable to even modest increases in potential flood hazard. The rising 21st century flood potential hazard from climate-driven increases in extreme precipitation is thus likely to be compounded by the so-called "expanding bulls-eye effect" (Ashley et al., 2013), whereby the growing geographic extent of populated urban and exurban areas produces a broader "target" for geophysical natural hazards. Such a reality points to the urgent need for targeted policy and land use interventions to guide future development away from these high risk zones (Johnson et al., 2020) and potentially also to consider alternative interventions (e.g., habitat restoration that increases floodwater storage) within present-day floodplains likely to be inundated with greater depth and frequency due to CC. Future increases in population exposure may also have a

disproportionate impact on vulnerable populations and disadvantaged communities, potentially exacerbating current inequities.

Finally, we emphasize that the disproportionately large projected increases in the most intense precipitation events (i.e., those with 50- to 200-year RIs) may be of particular concern from a catastrophe risk management perspective (Anenberg et al., 2019; Wright et al., 2019b). Major dams, bridges, and levees in urban areas are generally designed to withstand the worst plausible flood events—and our analysis assumes such infrastructure performs optimally as designed, with no structural failures. Yet, our findings point to the potential for relatively widespread occurrence of historically unprecedented extreme precipitation events in the coming decades—including some which will likely exceed those associated with historical 100- to 200-year RIs. Indeed, several examples of flood events exceeding contemporary "plausible worst case" estimates have occurred over the past decade in the CONUS—including the record-breaking deluge associated with Hurricane Harvey, which stalled near Houston, Texas in 2017 (e.g., Emanuel, 2017). Even lesser extreme precipitation events (i.e., those with historical RIs of 25–50 years) have recently resulted in damaging and life-threatening dam failures in the United States, including in the Upper Midwest in 2019 and Michigan in 2020. Thus, these projected increases in high-end precipitation extremes point to the critical importance of incorporating estimates of strongly nonstationary tail risks into design considerations for new civil engineering projects, as well as the growing need to reassess safety margins and emergency protocols for existing critical infrastructure.

Conflict of Interest

The authors have no competing interests to declare.

Data Availability Statement

All raw climate model and population data used in this analysis are presently available in existing public repositories. CESM-LENS precipitation data may be accessed online (http://www.cesm.ucar.edu/projects/community-projects/LENS/data-sets.html). Present-day (EnviroAtlas) and future (ICLUS) population data sets are available from the US EPA Environmental Dataset Gateway (https://edg.epa.gov). Fathom-US flood layers, and the data with which they are built, are available from Wing et al. (2017).

Acknowledgments

Swain was supported by a joint collaboration between the Institute of the Environment and Sustainability at the University of California, Los Angeles; the Center for Climate and Weather Extremes at the National Center for Atmospheric Research; and the Nature Conservancy of California. Johnson and Wing received partial support from the Kresge Foundation. This material is based upon work supported by the National Science Foundation under Grant Numbers 1854940 (Done) and 1854761 (Swain). Bates is supported by a Royal Society Wolfson Research Merit Award. The National Center for Atmospheric Research is sponsored by the National Science Foundation. Finally, we also acknowledge high-performance computing support provided by NCAR's Computational and Information Systems Laboratory, sponsored by the National Science Foundation.

References

de Almeida, G. A. M., Bates, P., Freer, J. E., & Souvignet, M. (2012). Improving the stability of a simple formulation of the shallow water equations for 2-D flood modeling. *Water Resources Research*, *48*, W05528. https://doi.org/10.1029/2011WR011570

Anenberg, S. C., Dutton, A., Goulet, C. A., Swain, D. L., & van der Pluijm, B. (2019). Toward a resilient global society: Air, sea level, earthquakes, and weather. *Earth's Future*, *7*, 854–864. https://doi.org/10.1029/2019EF001242

Ashley, W. S., Strader, S., Rosencrants, T., & Krmenec, A. J. (2013). Spatiotemporal changes in tornado hazard exposure: The case of the expanding bull's-eye effect in Chicago, Illinois. *Weather, Climate, and Society*, *6*(2), 175–193. https://doi.org/10.1175/WCAS-D-13-00047.1

Bacmeister, J. T., Reed, K. A., Hannay, C., Lawrence, P., Bates, S., Truesdale, J. E., et al. (2018). Projected changes in tropical cyclone activity under future warming scenarios using a high-resolution climate model. *Climatic Change*, *146*(3), 547–560. https://doi.org/10.1007/s10584-016-1750-x

Bates, P. D., Horritt, M. S., & Fewtrell, T. J. (2010). A simple inertial formulation of the shallow water equations for efficient two-dimensional flood inundation modelling. *Journal of Hydrology*, *387*(1), 33–45. https://doi.org/10.1016/j.jhydrol.2010.03.027

Brunner, M. I., Gilleland, E., Wood, A., Swain, D. L., & Clark, M. (2020). Spatial dependence of floods shaped by spatiotemporal variations in meteorological and land-surface processes. *Geophysical Research Letters*, e2020GL088000. https://doi.org/10.1029/2020GL088000

Davenport, F. V., Herrera-Estrada, J. E., Burke, M., & Diffenbaugh, N. S. (2020). Flood size increases nonlinearly across the Western United States in response to lower snow precipitation ratios. *Water Resources Research*, *56*, e2019WR025571. https://doi.org/10.1029/2019WR025571

Diffenbaugh, N. S. (2020). Verification of extreme event attribution: Using out-of-sample observations to assess changes in probabilities of unprecedented events. *Science Advances*, *6*(12), eaay2368. https://doi.org/10.1126/sciadv.aay2368

Diffenbaugh, N. S., Singh, D., Mankin, J. S., Horton, D. E., Swain, D. L., Touma, D., et al. (2017). Quantifying the influence of global warming on unprecedented extreme climate events. *Proceedings of the National Academy of Sciences*, *114*(19), 4881. https://doi.org/10.1073/pnas.1618082114

Du, H., Alexander, L. V., Donat, M. G., Lippmann, T., Srivastava, A., Salinger, J., et al. (2019). Precipitation from persistent extremes is increasing in most regions and globally. *Geophysical Research Letters*, *46*, 6041–6049. https://doi.org/10.1029/2019GL081898

Emanuel, K. (2017). Assessing the present and future probability of Hurricane Harvey's rainfall. *Proceedings of the National Academy of Sciences*, *114*(48), 12,681.

Ficklin, D. L., Abatzoglou, J. T., & Novick, K. A. (2019). A new perspective on terrestrial hydrologic intensity that incorporates atmospheric water demand. *Geophysical Research Letters*, *46*, 8114–8124. https://doi.org/10.1029/2019GL084015

Fowler, M. D., Kooperman, G. J., Randerson, J. T., & Pritchard, M. S. (2019). The effect of plant physiological responses to rising CO_2 on global streamflow. *Nature Climate Change*, *9*(11), 873–879. https://doi.org/10.1038/s41558-019-0602-x

Fuss, S., Canadell, J. G., Peters, G. P., Tavoni, M., Andrew, R. M., Ciais, P., et al. (2014). Betting on negative emissions. *Nature Climate Change*, *4*(10), 850–853. https://doi.org/10.1038/nclimate2392

Giorgi, F., Im, E. S., Coppola, E., Diffenbaugh, N. S., Gao, X. J., Mariotti, L., & Shi, Y. (2011). Higher Hydroclimatic intensity with global warming. *Journal of Climate*, *24*(20), 5309–5324. https://doi.org/10.1175/2011JCLI3979.1

Huang, X., Swain, D. L., & Hall, A. (2020). Large ensemble downscaling of extreme atmospheric river storms in California reveals large increase in fine-scale precipitation. *Science Advances*, *6*(29), eaba1323.

Johnson, K. A., Wing, O. E. J., Bates, P. D., Fargione, J., Kroeger, T., Larson, W. D., et al. (2020). A benefit–cost analysis of floodplain land acquisition for US flood damage reduction. *Nature Sustainability*, *3*(1), 56–62. https://doi.org/10.1038/s41893-019-0437-5

Kay, J. E., Deser, C., Phillips, A., Mai, A., Hannay, C., Strand, G., et al. (2015). The Community Earth System Model (CESM) Large Ensemble Project: A community resource for studying climate change in the presence of internal climate variability. *Bulletin of the American Meteorological Society*, *96*(8), 1333–1349. https://doi.org/10.1175/bams-d-13-00255.1

Kay, J. E., L'Ecuyer, T., Pendergrass, A., Chepfer, H., Guzman, R., & Yettella, V. (2018). Scale-aware and definition-aware evaluation of modeled near-surface precipitation frequency using CloudSat observations. *Journal of Geophysical Research: Atmospheres*, *123*, 4294–4309. https://doi.org/10.1002/2017JD028213

Kharin, V. V., Zwiers, F. W., Zhang, X., & Wehner, M. (2013). Changes in temperature and precipitation extremes in the CMIP5 ensemble. *Climatic Change*, *119*(2), 345–357. https://doi.org/10.1007/s10584-013-0705-8

Kossin, J. P. (2018). A global slowdown of tropical-cyclone translation speed. *Nature*, *558*(7708), 104–107. https://doi.org/10.1038/s41586-018-0158-3

Kundzewicz, Z. W., Kanae, S., Seneviratne, S. I., Handmer, J., Nicholls, N., Peduzzi, P., et al. (2014). Flood risk and climate change: Global and regional perspectives. *Hydrological Sciences Journal*, *59*(1), 1–28. https://doi.org/10.1080/02626667.2013.857411

Lehner, B., & Grill, G. (2013). Global river hydrography and network routing: Baseline data and new approaches to study the world's large river systems. *Hydrological Processes*, *27*(15), 2171–2186. https://doi.org/10.1002/hyp.9740

Lehner, B., Verdin, K., & Jarvis, A. (2008). New global hydrography derived from spaceborne elevation data, Eos. *Transactions American Geophysical Union*, *89*(10), 93–94. https://doi.org/10.1029/2008EO100001

Lenderink, G., Barbero, R., Loriaux, J. M., & Fowler, H. J. (2017). Super-Clausius–Clapeyron scaling of extreme hourly convective precipitation and its relation to large-scale atmospheric conditions. *Journal of Climate*, *30*(15), 6037–6052. https://doi.org/10.1175/JCLI-D-16-0808.1

Lochbihler, K., Lenderink, G., & Siebesma, A. P. (2019). Response of extreme precipitating cell structures to atmospheric warming. *Journal of Geophysical Research: Atmospheres*, *124*, 6904–6918. https://doi.org/10.1029/2018JD029954

Lopez-Cantu, T., Prein, A. F., & Samaras, C. (2020). Uncertainties in future U.S. extreme precipitation from downscaled climate projections. *Geophysical Research Letters*, *47*, e2019GL086797. https://doi.org/10.1029/2019GL086797

Mizuta, R., & Endo, H. (2020). Projected changes in extreme precipitation in a 60-km AGCM large ensemble and their dependence on return periods. *Geophysical Research Letters*, e2019GL086855. https://doi.org/10.1029/2019GL086855

Neal, J., Schumann, G., & Bates, P. (2012). A subgrid channel model for simulating river hydraulics and floodplain inundation over large and data sparse areas. *Water Resources Research*, *48*, W11506. https://doi.org/10.1029/2012WR012514

Neelin, J. D., Sahany, S., Stechmann, S. N., & Bernstein, D. N. (2017). Global warming precipitation accumulation increases above the current-climate cutoff scale. *Proceedings of the National Academy of Sciences*, *114*(6), 1258–1263. https://doi.org/10.1073/pnas.1615333114

Norris, J., Chen, G., & Neelin, J. D. (2019). Changes in frequency of large precipitation accumulations over land in a warming climate from the CESM large ensemble: The roles of moisture, circulation, and duration. *Journal of Climate*, *32*(17), 5397–5416. https://doi.org/10.1175/JCLI-D-18-0600.1

Papalexiou, S. M., Koutsoyiannis, D., & Makropoulos, C. (2013). How extreme is extreme? An assessment of daily rainfall distribution tails. *Hydrology and Earth System Sciences*, *17*(2), 851–862. https://doi.org/10.5194/hess-17-851-2013

Pendergrass, A. G., Coleman, D. B., Deser, C., Lehner, F., Rosenbloom, N., & Simpson, I. R. (2019). Nonlinear response of extreme precipitation to warming in CESM1. *Geophysical Research Letters*, *46*, 10,551–10,560. https://doi.org/10.1029/2019GL084826

Pendergrass, A. G., Knutti, R., Lehner, F., Deser, C., & Sanderson, B. M. (2017). Precipitation variability increases in a warmer climate. *Scientific Reports*, *7*(1), 17966. https://doi.org/10.1038/s41598-017-17966-y

Polade, S. D., Pierce, D. W., Cayan, D. R., Gershunov, A., & Dettinger, M. D. (2014). The key role of dry days in changing regional climate and precipitation regimes. *Scientific Reports*, *4*, 4364. https://doi.org/10.1038/srep04364

Prein, A. F., Liu, C., Ikeda, K., Bullock, R., Rasmussen, R. M., Holland, G. J., & Clark, M. (2017). Simulating North American mesoscale convective systems with a convection-permitting climate model. *Climate Dynamics*, *55*(1-2), 95–110. https://doi.org/10.1007/s00382-017-3993-2

Prein, A. F., Liu, C., Ikeda, K., Trier, S. B., Rasmussen, R. M., Holland, G. J., & Clark, M. P. (2017). Increased rainfall volume from future convective storms in the US. *Nature Climate Change*, *7*(12), 880–884. https://doi.org/10.1038/s41558-017-0007-7

Rogelj, J., den Elzen, M., Höhne, N., Fransen, T., Fekete, H., Winkler, H., et al. (2016). Paris agreement climate proposals need a boost to keep warming well below 2 °C. *Nature*, *534*(7609), 631–639. https://doi.org/10.1038/nature18307

Sampson, C. C., Bates, P. D., Neal, J. C., & Horritt, M. S. (2013). An automated routing methodology to enable direct rainfall in high resolution shallow water models. *Hydrological Processes*, *27*(3), 467–476. https://doi.org/10.1002/hyp.9515

Sampson, C. C., Smith, A. M., Bates, P. D., Neal, J. C., Alfieri, L., & Freer, J. E. (2015). A high-resolution global flood hazard model. *Water Resources Research*, *51*, 7358–7381. https://doi.org/10.1002/2015WR016954

Sharma, A., Wasko, C., & Lettenmaier, D. P. (2018). If precipitation extremes are increasing, why aren't floods? *Water Resources Research*, *54*, 8545–8551. https://doi.org/10.1029/2018WR023749

Smith, A., Sampson, C., & Bates, P. (2015). Regional flood frequency analysis at the global scale. *Water Resources Research*, *51*, 539–553. https://doi.org/10.1002/2014WR015814

Stephens, G. L., L'Ecuyer, T., Forbes, R., Gettelmen, A., Golaz, J.-C., Bodas-Salcedo, A., et al. (2010). Dreary state of precipitation in global models. *Journal of Geophysical Research*, *115*, D24211. https://doi.org/10.1029/2010JD014532

Swain, D. L., Langenbrunner, B., Neelin, J. D., & Hall, A. (2018). Increasing precipitation volatility in twenty-first-century California. *Nature Climate Change*, *8*(5), 427–433. https://doi.org/10.1038/s41558-018-0140-y

Swain, D. L., Singh, D., Touma, D., & Diffenbaugh, N. S. (2020). Attributing extreme events to climate change: A new frontier in a warming world. *One Earth*, *2*(6), 522–527.

Swain, D. L., Tsiang, M., Haugen, M., Singh, D., Charland, A., Rajaratnam, B., & Diffenbaugh, N. S. (2014). The extraordinary California drought of 2013/2014: Character, context, and the role of climate change. *Bulletin of the American Meteorological Society*, *95*(9), S3–S7.

Thackeray, C. W., DeAngelis, A. M., Hall, A., Swain, D. L., & Qu, X. (2018). On the connection between global hydrologic sensitivity and regional wet extremes. *Geophysical Research Letters*, *45*, 11,343–311,351. https://doi.org/10.1029/2018GL079698

Touma, D., Michalak, A. M., Swain, D. L., & Diffenbaugh, N. S. (2018). Characterizing the spatial scales of extreme daily precipitation in the United States. *Journal of Climate*, *31*(19), 8023–8037. https://doi.org/10.1175/jcli-d-18-0019.1

Touma, D., Stevenson, S., Camargo, S. J., Horton, D. E., & Diffenbaugh, N. S. (2019). Variations in the intensity and spatial extent of tropical cyclone precipitation. *Geophysical Research Letters*, *46*, 13,992–14,002. https://doi.org/10.1029/2019GL083452

Trenberth, K. E., Dai, A., Rasmussen, R. M., & Parsons, D. B. (2003). The changing character of precipitation. *Bulletin of the American Meteorological Society*, *84*(9), 1205–1217. https://doi.org/10.1175/BAMS-84-9-1205

Tye, M. R., & Cooley, D. (2015). A spatial model to examine rainfall extremes in Colorado's front range. *Journal of Hydrology*, *530*, 15–23. https://doi.org/10.1016/j.jhydrol.2015.09.023

U.S. EPA (Environmental Protection Agency). (2016) Updates to the Demographic and Spatial Allocation Models to Produce Integrated Climate and Land Use Scenarios (ICLUS) Version 2. National Center for Environmental Assessment, Washington, DC; EPA/600/R-16/366F. Available from the National Technical Information Service, Springfield, VA, and online at http://www.epa.gov/ncea

Uhe, P. F., Mitchell, D. M., Bates, P. D., Sampson, C. C., Smith, A. M., & Islam, A. S. (2019). Enhanced flood risk with 1.5 °C global warming in the Ganges–Brahmaputra–Meghna basin. *Environmental Research Letters*, *14*(7), 074031. https://doi.org/10.1088/1748-9326/ab10ee

USDA (1986). Urban Hydrology for Small Watersheds, TR-55.

Villarini, G., Lavers, D. A., Scoccimarro, E., Zhao, M., Wehner, M. F., Vecchi, G. A., et al. (2014). Sensitivity of tropical cyclone rainfall to idealized global-scale forcings. *Journal of Climate*, *27*(12), 4622–4641. https://doi.org/10.1175/JCLI-D-13-00780.1

van Vuuren, D. P., Edmonds, J., Kainuma, M., Riahi, K., Thomson, A., Hibbard, K., et al. (2011). The representative concentration pathways: An overview. *Climatic Change*, *109*(1), 5. https://doi.org/10.1007/s10584-011-0148-z

Wing, O. E. J., Bates, P. D., Neal, J. C., Sampson, C. C., Smith, A. M., Quinn, N., et al. (2019). A new automated method for improved flood defense representation in large-scale hydraulic models. *Water Resources Research*, *55*, 11,007–11,034. https://doi.org/10.1029/2019WR025957

Wing, O. E. J., Bates, P. D., Sampson, C. C., Smith, A. M., Johnson, K. A., & Erickson, T. A. (2017). Validation of a 30 m resolution flood hazard model of the conterminous United States. *Water Resources Research*, *53*, 7968–7986. https://doi.org/10.1002/2017WR020917

Wing, O. E. J., Sampson, C. C., Bates, P. D., Quinn, N., Smith, A. M., & Neal, J. C. (2019). A flood inundation forecast of Hurricane Harvey using a continental-scale 2D hydrodynamic model. *Journal of Hydrology*, *4*, 100039. https://doi.org/10.1016/j.hydroa.2019.100039

Wright, D. B., Bosma, C. D., & Lopez-Cantu, T. (2019a). U.S. hydrologic design standards insufficient due to large increases in frequency of rainfall extremes. *Geophysical Research Letters*, *46*, 8144–8153. https://doi.org/10.1029/2019GL083235

Wright, D. B., Bosma, C. D., & Lopez-Cantu, T. (2019b). U.S. hydrologic design standards insufficient due to large increases in frequency of rainfall extremes. *Geophysical Research Letters*, *0*, 8144–8153. https://doi.org/10.1029/2019GL083235

Zhang, G., Murakami, H., Knutson, T. R., Mizuta, R., & Yoshida, K. (2020). Tropical cyclone motion in a changing climate. *Science Advances*, *6*(17), eaaz7610. https://doi.org/10.1126/sciadv.aaz7610